Damage pattern recognition for corroded beams strengthened by CFRP anchorage system based on acoustic emission techniques

Pan, Tanbo; Zheng, Yonglai; Zhou, Yubao; Luo, Wenbin; Xu, Xubing; Hou, Chenyu; Zhou, Yujue

DOI
10.1016/j.conbuildmat.2023.133474

Publication date
2023

Document Version
Final published version

Published in
Construction and Building Materials

Construction and Building Materials 406 (2023) 133474

Contents lists available at ScienceDirect

Construction and Building Materials

journal homepage: www.elsevier.com/locate/conbuildmat

Damage pattern recognition for corroded beams strengthened by CFRP anchorage system based on acoustic emission techniques

Tanbo Pan [a], Yonglai Zheng [a], Yubao Zhou [c,*], Wenbin Luo [a], Xubing Xu [a], Chenyu Hou [a], Yujue Zhou [a,b]

[a] Department of Hydraulic Engineering, Civil Engineering College, Tongji University, China
[b] Department of Civil Engineering, Sanming University, China
[c] Faculty of Civil Engineering and Geosciences, Delft Univerisity of Technology, Netherlands

ARTICLE INFO

Keywords:
Acoustic emission
CFRP anchorage system
Damage pattern recognition
Damage mechanism

ABSTRACT

This study presents a damage pattern recognition approach for corroded steel beams strengthened by CFRP anchorage system based on acoustic emission clustering analysis. The proposed method includes four steps: acoustic emission signal acquisition, feature extraction, clustering analysis, and damage pattern recognition. Four corroded beams with different corrosion levels and strengthening schemes were tested under four-point bending loading. The acoustic emission signals were collected during the loading process and analyzed using Gaussian mixture model clustering method. The results showed that the collected AE data were analyzed using clustering analysis, successfully distinguishing the distinct damage patterns associated with each mode. The AE signals exhibited distinct characteristics for different damage modes: concrete matrix damage had high-frequency and low-energy characteristics, CFRP-matrix debonding showed intermediate values for all parameters, and CFRP tearing had longer durations, lower peak frequencies, and high-energy characteristics. Besides, the study identified three stages of the damage process: an initial stage with fewer low-intensity AE signals, a damage development stage characterized by an increase in concrete-matrix damage and CFRP – matrix debonding signals, and a continuous damage growth stage with significant AE signals associated with three damage modes. Furthermore, the degree of corrosion significantly influenced the cumulative AE energy of damage modes. Lower degrees of corrosion led to higher cumulative energy from concrete matrix damage and CFRP-matrix debonding. These findings provide valuable insights for understanding the damage evolution and failure mechanisms of CFRP-strengthened corroded beams. The use of AE techniques for damage pattern recognition can enhance the evaluation and design of CFRP anchorage systems, leading to more effective rehabilitation strategies for corroded structures.

1. Introduction

Corrosion is a significant problem for steel structures as it can lead to reduced load carrying capacity and ultimately, structural failure. [1,2] Therefore, several techniques have been developed for the rehabilitation of corroded steel structures. Some of these techniques include traditional methods such as patch repair, plate bonding, and cathodic protection, while others include more advanced techniques such as the use of fiber-reinforced polymers (FRPs) [3–8].

Due to the advantages of FRP, such as light weight, high strength, corrosion resistance, high designability, and ease of construction and molding, FRP has become a major complement to traditional materials such as concrete in the field of civil engineering [9–12]. The utilization of FRP-concrete combination structures effectively leverages the compressive capacity of concrete and the high tensile strength of FRP. This approach reduces structural self-weight, enhances durability, and provides a solution to longstanding challenges in reinforcing and repairing concrete structures [13–16]. Noteworthy, premature debonding damage of FRP ends is the most commonly-encountered failure mode in FRP-concrete combination structures without reaching the ultimate strength of the fibers. It was observed that the FRP sheets may debond at 50% or less of their ultimate tensile strength, that reduces the efficiency of the strengthening system [17]. FRP anchors, as a new anchorage method, can not only avoid or control the premature

* Corresponding author.
E-mail address: Y.Zhou-16@tudelf.nl (Y. Zhou).

https://doi.org/10.1016/j.conbuildmat.2023.133474
Received 22 July 2023; Received in revised form 17 September 2023; Accepted 19 September 2023
Available online 25 September 2023

debonding of FRP sheet, but also greatly improve the efficiency of fiber utilization.

Since the FRP composite structure is a combination of FRP sheet, FRP anchors and reinforced concrete, its force characteristics and damage mechanism are more intricate than for RC structures [18–20]. To completely clarify the damage mechanism of FRP composite structures, all damage mechanism, such as matrix cracking, the fiber–matrix debonding, the fiber breakage, must be elucidated, which poses a challenge to the analysis of the damage mechanism of FRP composite structures. Acoustic emission (AE) technology is a real-time, non-damage monitoring technique, which can effectively detect and record transient elastic waves emitted from internal damages by sensors attached to the surface of the structure [21–24], which is a superior means of damage analysis.

Currently, there are two main methods to process the AE signals: parameter-based and waveform-based analyses. The parametric analysis method usually uses waveform characteristic parameters such as amplitude, ring count, and energy to characterize different damage modes, which is simple, good in real time and easy to operate. Degala et al. [25] conducted an AE study of CFRP-strengthened concrete slabs under four-point bending test and results showed that the AE parameters, including amplitude, energy, and ringing counts can effectively characterize the failure modes of CFRP-strengthened RC slabs. Barrell et al. [26] showed that damage with a small effect on the overall mechanical properties of the material, such as matrix cracking, was accompanied by a low-amplitude AE signal, while damage with a large effect, such as fiber fracture, was accompanied by a high-amplitude AE signal. Shahidan et al. [27]conducted experiments involving four-point bending tests on reinforced concrete (RC) beams. They employed RA analysis, calculated as the ratio of rise time to amplitude, as well as AF analysis, determined as the ratio of ringing counts to duration, to identify various crack types that developed in the beams at different stages of the testing process. Yu et al. [28] investigated the AE signals of fiber reinforced composite materials during fracture process, and obtained the spectral characteristics of fiber fracture by simultaneous observation with polarized light microscopy. Groot et al. [29] investigated real-time frequency determination of acoustic emission for different fracture mechanisms in carbon epoxy composites. It was found that the signal frequency of matrix cracking release was between 90 and 180 kHz, the signal frequency of fiber breakage was higher than 300 kHz, the signal frequency of fiber–matrix debonding was between 240 and 310 kHz, and the signal frequency of fiber pulling was between 180 and 240 kHz. (concluded that matrix cracking released frequencies between 90 and 180 kHz, fiber failure frequencies above 300 kHz, debonding frequencies between 240 and 310 kHz and pull-out frequencies between 180 and 240 kHz. Although certain features of the AE signal of the damage mechanism can be obtained by parametric analysis and spectral analysis, the overlap of parameter distributions between different damage modes makes it impossible to completely distinguish all damage modes by using only certain parameters as features. Therefore, there is an urgent need for AE analytical methods with stronger analytical capabilities.

With the rapid development of artificial intelligence technologies, the application of pattern recognition methods in AE signal analysis has gradually emerged. Pattern recognition methods can be divided into two categories: unsupervised and supervised, depending on whether the object classification of study is known or not. Cluster analysis is a representative of unsupervised pattern recognition methods, which classify patterns based on pattern characteristics and similarity measures. Several studies have used pattern recognition algorithms to group AE signals with similar characteristics and use these groupings to distinguish between damage states [30,31]. Johnson et al. [32] analyzed the AE transients in composite laminate tensile test specimens by principal component analysis (PCA). The unsupervised cluster analysis results showed that AE damage features from matrix cracking and local delamination can be separated in different clusters. Pei et al. [33] used the fuzzy c-means clustering algorithm to classify the AE events into three clusters which correspond to three damage modes of carbon/glass fiber-reinforced hybrid laminate composite specimens with different structure and indentation. Guo et al. [34] performed principal component analysis and K-means clustering analysis using relevant AE characteristic parameters (including energy, amplitude and duration) to identify various fatigue damage modes of carbon fiber/epoxy composite laminates with symmetrical architecture. Sause et al. [35] applied the validity analysis of clustering to determine the optimal number of clusters for the AE data, and the number of clusters obtained was consistent with the number of damage types of the CFRP samples. It can be found that pattern recognition technology represented by cluster analysis shows a powerful signal analysis capability with high recognition rate and intelligence, which has become an effective means for composite structure damage pattern recognition and damage mechanism exploration. Du et al. [36] investigated the damage evaluation and pattern recognition for the FRP/steel-confined RC column using the fuzzy C-means (FCM) algorithm and particle swarm optimization (PSO) algorithm. It was found that five damage mechanisms were identified and their typical damage waveforms were extracted. Nair et al. [37,38] applied unsupervised k-means clustering analysis, and the supervised neural networks to automatically cluster and separate the AE patterns of CFRP retrofitted RC beams.

While AE technique has been widely used in damage monitoring of steel structures, the application of AE in FRP-reinforced structures is still limited. Moreover, there is a lack of experimental studies on the identification and monitoring of damage modes in FRP-reinforced corroded structures, which is crucial for the maintenance and safety assessment of existing structures. Therefore, the development of effective AE-based damage pattern recognition methods for FRP-reinforced corroded structures is of great significance for enhancing the durability and safety of these structures.

This paper presents a novel approach for damage pattern recognition of corroded RC beams strengthened with a CFRP anchorage system based on clustering analysis of AE signals. The study aims to investigate the potential of the AE technique for monitoring the damage evolution in such structures, and develops a clustering analysis-based approach for damage pattern recognition of AE signals. Furthermore, the study analyses the correlation between the identified damage patterns and the corrosion level of the specimens. The contributions of this research include providing a novel approach for damage pattern recognition of FRP-reinforced structures, enhancing the understanding of the performance of FRP-reinforced corroded structures, and improving the reliability and efficiency of the AE technique for monitoring the health of RC structures.

2. Experimental setup and data acquisition

2.1. Materials and specimens

Four reinforced concrete (RC) beams were cast with cross-sectional dimensions of 150 mm × 200 mm × 1600 mm. The concrete was made using a design mix proportion of 1:1.65:2.52 (cement: sand: aggregate proportions by volume) and a water-to-cement ratio (w/c) of 0.47 (water: cement proportion by weight) [39]. The beams were constructed with a 25-millimeter-thick concrete cover. To enhance tensile strength, two D14 (14-millimeter diameter) steel bars with a total length of 1800 mm were employed at the bottom. For installation purposes, two D8 (8-millimeter diameter) steel bars, also with a total length of 1800 mm, were used at the top. Furthermore, evenly spaced D6 (6-millimeter diameter) steel bars were employed as stirrups, with an 80-millimeter spacing, to provide additional reinforcement, further strengthening the beam's structural integrity. Epoxy resin was used to cover the contact position between the stirrups and longitudinal tensile bars to prevent corrosion of the stirrups. Fig. 1 illustrates the dimensions and reinforcement details of RC beams.

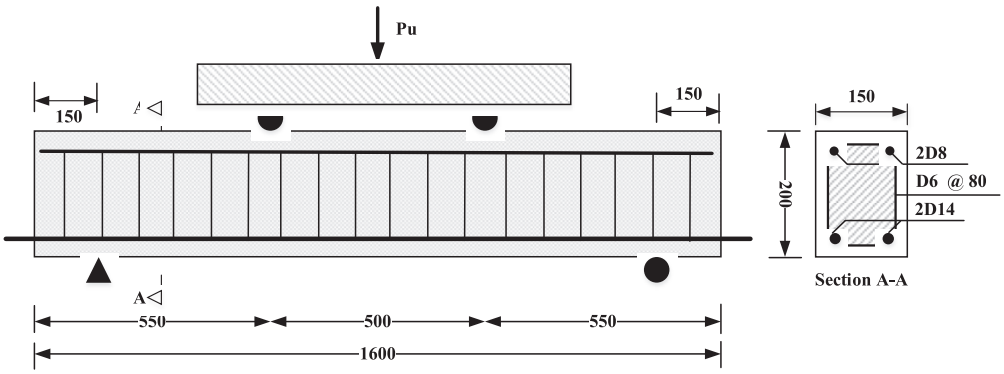

Fig. 1. Dimensions and reinforcement details of RC beams.

The mechanical properties of the materials used are summarized in Table 1. The concrete used had a compressive strength of 42.5 MPa with a standard deviation of 3.6 MPa. The longitudinal bars used had yield strengths of 462.2 MPa (with a standard deviation of 15.2 MPa) and 408.9 MPa (with a standard deviation of 5.5 MPa), and ultimate strengths of 615.7 MPa (with a standard deviation of 16.2 MPa) and 611.3 MPa (with a standard deviation of 4.5 MPa), respectively. The elastic modulus of the bars was 200 GPa. The CFRP sheet used had a thickness of 1.02 mm, a tensile strength of 3000 MPa, an elastic modulus of 230 GPa, and an ultimate strain of 1.66%, as provided by the manufacturer.

2.2. Corrosion treatment

Accelerated corrosion tests were conducted using an electrochemical method to obtain RC beams with different degrees of corrosion. To perform the electrochemical corrosion test, the specimens were placed on a corrosion trough with the exposed reinforcement bars outside the trough. A 5% NaCl solution was used as the electrolyte, and a constant DC voltage source (eTM-305F, with a voltage range of 0–30 V and a current range of 0–5 A) was used to provide the required voltage and current for the corrosion process. The tensile steel bars were made anode and connected to the positive terminal of the power supply, while the concrete was wrapped with a wire mesh outside, which was made cathode and connected to the negative terminal of the power supply. Furthermore, it is important to monitor the liquid level in the corrosion trough and promptly add more solution as needed to maintain a 5% concentration of NaCl, as the solution may evaporate faster in high temperature conditions.

To achieve different degrees of corrosion, different durations of electrochemical corrosion were applied to the reinforce16ment bars. The duration of corrosion was determined by Faraday's second law. According to Faraday's law, the amount of corrosion products is proportional to the quantity of electricity passing through the corroding steel. Thus, the corrosion time required to obtain a certain amount of corrosion can be calculated based on the amount of electricity passed through the steel and the charge needed for the formation of iron oxide. The theoretical mass loss is defined by Eq. (1).

Table 1
Mechanical properties of concrete, steel bars, concrete and CFRP sheets.

Materials	Strength and strain		Elastic modulus
Concrete	Compressive strength	42.5 ± 3.6 MPa	—
D14	Yield strength	615.7 ± 16.2 MPa	200GPa
	Ultimate strength	462.2 ± 5.5 MPa	
D8	Yield strength	611.3 ± 15.2 MPa	200GPa
	Ultimate strength	408.9 ± 4.5 MPa	
CFRP	Tensile strength	3000 MPa	230GPa
	Ultimate strain	1.66%	

$$\text{Mass loss} = \frac{ItM}{Fn} \tag{1}$$

Where t is the time elapsed (s); M is the atomic weight (for iron: M = 55.84 g/mol); n is the ion charge; and F is Faraday's constant, equal to 96,485C/mol, which is the amount of electrical charge in 1 mol of the metal; a constant electric current denoted as I was maintained at a current density of 180 $\mu A/cm^2$.

As previously mentioned, the corrosion time was set to 25, 50, and 100 days to induce mild, moderate, and severe corrosion damage, corresponding to the corrosion levels of 5%, 10%, and 20%, respectively. The beams were labeled as C0, C5, C10, and C20, in accordance with these corrosion levels.

2.3. CFRP anchorage system strengthening

2.3.1. Fabrication of CFRP anchors

The manufacturing method of CFRP anchors typically involves several steps [40,41]. First, a suitable unidirectional CFRP sheet is selected and cut to the required dimensions, with a width of 150 mm and a length of 80 mm. The 80 mm length is then divided into two sections, a 50 mm fan-shaped section and a 30 mm pre-built section that includes a small margin for a 90-degree bend section. A 10 mm dowel is inserted into the fan-shaped section to form the main body of the anchor. According to Llauradó [41], the hardened length of the anchor should not exceed two-thirds of the embedment length to prevent damage to the bending area. Therefore, epoxy is applied to an end part spanning ten millimeters over the entire width of the sheet to produce the hardened shaft. A small margin is left in the pre-built 30 mm section to form a 90-degree bend section, which creates a bendable area between the main body and the hardened section of the CFRP anchor. Finally, to create bow-tie CFRP anchors, two different lengths of CFRP sheet are cut and the above steps are followed to create the main body, hardened section and bending section of the anchor. The detailed construction process was illustrated in Fig. 2.

2.3.2. Strengthening procedure

The CFRP anchorage system strengthening procedure involves the following steps:

a) Surface preparation: To prepare the surface of weakened concrete for reinforcement, a pneumatic needle scaler was used to roughen the

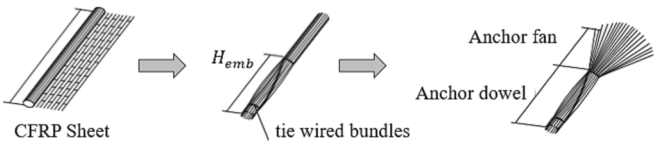

Fig. 2. The construction process of CFRP anchors.

surface and remove the top layer of concrete. This process exposed the aggregates across the area where the CFRP sheets were to be bonded, creating a textured surface that is conducive to bonding. This type of surface preparation is critical in ensuring the strong adhesion of the CFRP sheets to the concrete surface, and ultimately, the effectiveness of the reinforcement.

b) Hole drilling: Four holes were drilled into the bottom faces of the beams using a diamond-tipped drill bit with a diameter of 10 mm and a depth of 35 mm. The location of the anchor holes was marked on the beam surface prior to drilling for accuracy. To ensure better adherence between the concrete surface and epoxy resin, pressurized air and a vacuum were used to remove concrete particles and dust from the drilled holes and the bottom surface of the beams.
c) CFRP sheet application: epoxy resin was applied to the surface of the RC beams to be reinforced, and the fabricated CFRP sheets were quickly pasted on it. A small amount of epoxy resin was applied evenly on the surface of the CFRP sheet and squeezed several times along the direction of the CFRP sheet texture with a roller to remove air bubbles.
d) Anchor installation: The CFRP anchoring rods were inserted into the drilled holes, leaving the predetermined anchoring depth protruding from the beam surface, as illustrated in Fig. 3 (b). A small amount of epoxy adhesive was applied to the anchor rod before installation to enhance the bond strength between the rod and the concrete.
e) Curing: The curing time of the epoxy adhesive and CFRP sheets was allowed according to the manufacturer's instructions, usually 7 days, to ensure the adhesive reaches maximum strength.

By following these steps, the CFRP anchorage system can effectively increase the load capacity and extend the service life of corroded beams. The CFRP anchorage system is lightweight, easy to install, and has excellent durability, making it a reliable solution for the repair and reinforcement of corroded beams.

2.4. Load testing and AE monitoring

The loading test was conducted at the Laboratory of Engineering Structural Performance Evolution and Control, Tongji University, using an electro-hydraulic servo testing machine with a maximum load capacity of 2,000 kN. Two pre-loading was performed before the formal loading, and the pre-loading value was 5% of the theoretical calculated ultimate load of the beam to ensure close contact between the loading device and the RC beam. Thereafter, a displacement-controlled loading scheme with a loading rate of 1 mm/min was utilized until the specimen failed. During the loading process, high-definition cameras were used to record the whole process on both sides of the loaded test beam, which facilitated accurate observation of the crack development and failure mode of the RC beams.

AE monitoring setups conform to international standards for acoustic emission monitoring in concrete structures [42]. AE signal acquisition was performed using a 16-channel Micro-II Express Digital AE system, provided by Mistras Group, Inc. A constant threshold of 40 dB and a pre-amplification of 40 dB were implemented. The pre-trigger and sampling rate were initialized at 256 microseconds and 5 MHz, respectively. To optimize signal detection, all sensors were equipped with a band-pass filter ranging from 20 kHz to 400 kHz, which is consistent with the expected frequency range for most detected AE signals in concrete [43]. The hit lock time and hit definition time were 300us and 1000us, respectively. Five broadband, resonant-type, single-crystal piezoelectric transducers from Physical Acoustics Corporation (PAC), called PICO, were used as the AE sensors. As shown in Fig. 4, three sensors were evenly arranged near the top of the beam (two at the end and one in the middle), and the remaining two sensors were placed at the bottom of the beam. Before the actual AE monitoring, the AE sensors were checked for sensitivity using pencil lead break test. The AE signals were recorded continuously during the flexural testing of RC beams corroded to different ages during the entire duration of loading.

3. Clustering methodology

The Gaussian Mixture Model (GMM), an unsupervised learning algorithm, has been widely used in grouping data into clusters. A GMM is a parametric probability density function represented as a weighted sum of Gaussian component densities [44–46]. The model is trained using the Expectation Maximization (EM) algorithm, and most parameters are adjusted automatically. The expectation is maximized by iteratively updating the mean μ and standard deviation σ of the distribution until the variation in these two parameters is very small. Therefore, the AE signal to be clustered can be viewed as a number of joint probability distributions from multiple Gaussian distributions. The GMM (or the linear superposition of Gaussians) is expressed as Eq. (2).

$$p(x) = \sum_{k=1}^{K} \pi_k N(x|\mu_k, \Sigma_k) \tag{2}$$

Where K is the desired number of Gaussians or number clusters), $\sum_{k=1}^{K} N(x|\mu_k, \Sigma_k)$ is a normal multivariate Gaussian distribution of class, π_k is the k^{th} weight coefficient of Gaussian density functions. A D- variate Gaussian distribution function is given in Eq. (3).

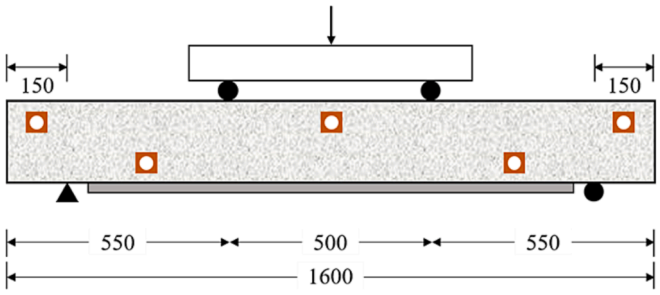

Fig. 4. Layout of the AE sensors.

(a) Hole drilling (b) Anchor installation (c) Curing

Fig. 3. Anchors installation procedure.

$$N\left(x\middle|\mu_k,\sum_k\right)=\frac{1}{(2\pi)^{D/2}|\sum|^{1/2}}e^{\frac{-1}{2}}\left[(x-\mu)^T\sum^{-1}(x-\mu)\right] \tag{3}$$

Where μ_k is the mean vector of k^{th} Gaussian density functions; Σ_k is the covariance matrix of k^{th} Gaussian density functions.

The mixing coefficient (or weightage) satisfies the constraint $0 \leq \pi k \leq 1$ and is given in Eq. (4).

$$\sum_{k=1}^{K}\pi_k=1 \tag{4}$$

For a univariate Gaussian distribution, the probability density function [F(x)] is given in Eq. (5).

$$F(x)=G(x|\mu,\sigma)=\frac{1}{\sqrt{2\pi\sigma^2}}e^{\frac{-1}{2}\left(\frac{x-\mu}{\sigma}\right)^2} \tag{5}$$

Where - $\infty \leq x \leq \infty$, μ is the mean, and σ is the standard deviation of the data. Standard deviation (σ) can be thought of measuring how far the data values lie from the mean (μ). Assuming that the variables are independent with probability density function's $N(\mu_1,\sigma_1^2), N(\mu_2,\sigma_2^2), \cdots, N(\mu_P,\sigma_P^2)$, respectively. The joint densities are given by Eq. (6).

$$F(x_1,x_2,\cdots x_P)=f(x_1)\cdot f(x_2)\cdot\cdots\cdot f(x_P) \tag{6}$$

The variance and standard deviation describe how spread out the data are. If the data all lie close to the mean, then the standard deviation is small, whereas if the data are spread out over large range of values, σ is large. Solving Equation A5:

$$F(x_1,x_2,\cdots x_P)=\frac{1}{(2\pi)^{P/2}(\sigma_1^2\sigma_2^2\cdots\sigma_P^2)^{1/2}}e^{\frac{-1}{2}}\left[\left(\frac{x_1-\mu_1}{\sigma_1}\right)^2+\cdots+\left(\frac{x_P-\mu_P}{\sigma_P}\right)^2\right] \tag{7}$$

4. Data preprocessing and cluster analysis

4.1. Data preprocessing and feature selection

The AE signal collected by an AE acquisition system can been represented by a set of characteristic parameters, including rise time, count, amplitude, average frequency, center of mass frequency, duration, peak frequency, signal strength, etc. Selecting appropriate parameters for cluster analysis can greatly simplify the clustering calculation process. The parameters used for clustering analysis should not only describe the majority of the information in the AE signal waveform, but also exclude the interference of unrelated parameters. Therefore, correlation analysis was adopted to select the AE characteristic parameters. Correlations were evaluated using the spearman correlation test: the spearman coefficient was considered to indicate poor correlation if < 0.2, moderate if < 0.4, relatively strong if < 0.6, strong if < 0.8, and very strong if > 0.8.

Fig. 5 shows the correlation coefficient matrix of each AE parameter. It can be observed that there is a strong correlation between the ring count, duration, and amplitude. Additionally, there is a strong correlation between absolute energy, energy, and signal intensity, as well as between backcalculation frequency and average frequency. Furthermore, it is worth noting that some studies have shown that AE parameters, such as rise time, ringing counts, energy, duration, and amplitude, can be used to assess the development of damage cracks in the sample. By utilizing parameter correlation analysis, it is possible to reduce the subset of acoustic emission descriptors and subsequently decrease computational workload, leading to improved clustering results. After conducting a correlation analysis, the parameter set was reduced to five parameters: AE ring counts, rise time, average frequency, absolute energy, and peak frequency. These parameters were then utilized in principal component analysis and cluster analysis.

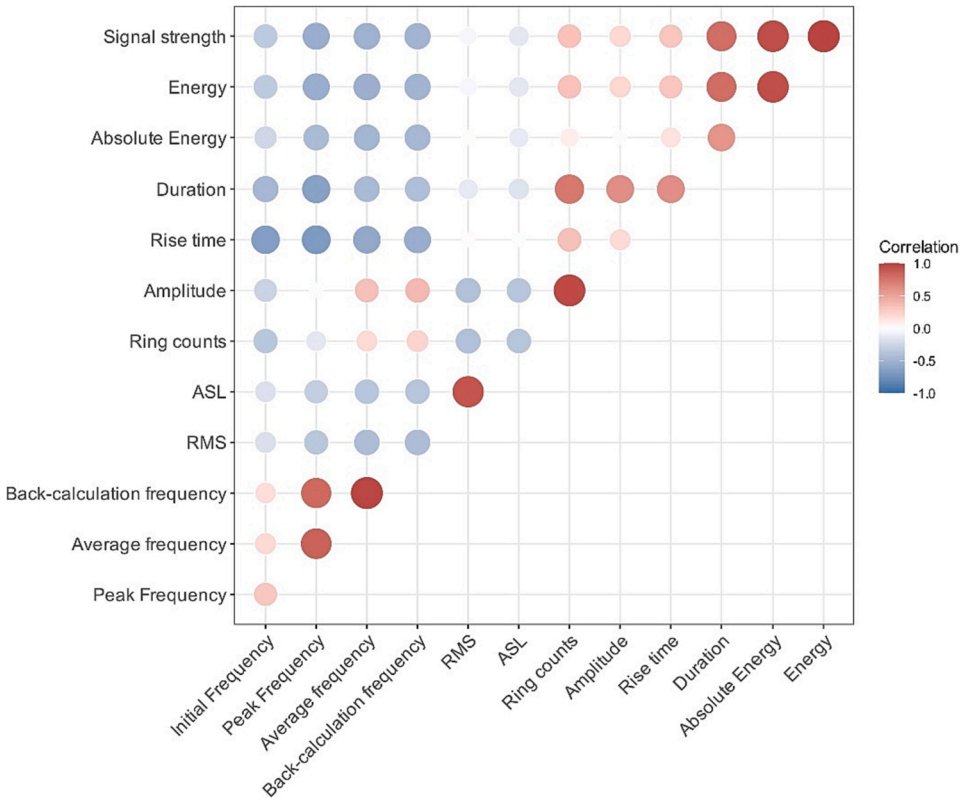

Fig. 5. Correlation coefficient matrix of each AE parameter.

4.2. Principal component analysis

Before performing principal component analysis on the AE data, the sample values were normalized to a range of 0 to 1. The Z-score method was used for data normalization, which can accelerate the convergence of the model parameters during training and improves learning accuracy.

$$z = \frac{x - \mu}{\sigma} \tag{8}$$

Where μ and σ denote the mean and standard deviation of each column, respectively.

The key to conducting principal component analysis is to determine the number of new composite parameters that can describe all the characteristic information of the original AE signal parameters to the greatest extent possible, while minimizing the number of new parameters [47–49]. Therefore, PCA analyses are employed to recombine AE characteristic parameters, including rise time, count, energy, duration, amplitude, amplitude frequency, signal strength, central frequency, and peak frequency, which have a certain relevance, to form a new set of independent characteristics. Besides, the required number of principal components was determined by introducing the contribution of eigenvalues and cumulative eigenvalues contribution rate, which can reflect the comprehensive ability of the original feature parameters.

Fig. 6 illustrates the eigenvalues and their contributions. It is apparent that the first principal component accounted for 50.0% of the total variation, and the second principal component contributed 38.30%. Given that the cumulative contribution rate of the first two principal components reached 88.3% and the eigenvalues exceeded 1, the first two new integrated parameters already contain the main information characteristics of the original AE signal parameters. Therefore, the first two principal components, PCA1 and PCA2, have been deliberately chosen. These components symbolize fresh attributes extracted through PCA analysis, residing within a transformed coordinate framework. They are amenable for delving into the analysis of the interrelationship among volatile constituents within CFRP-reinforced corroded beams.

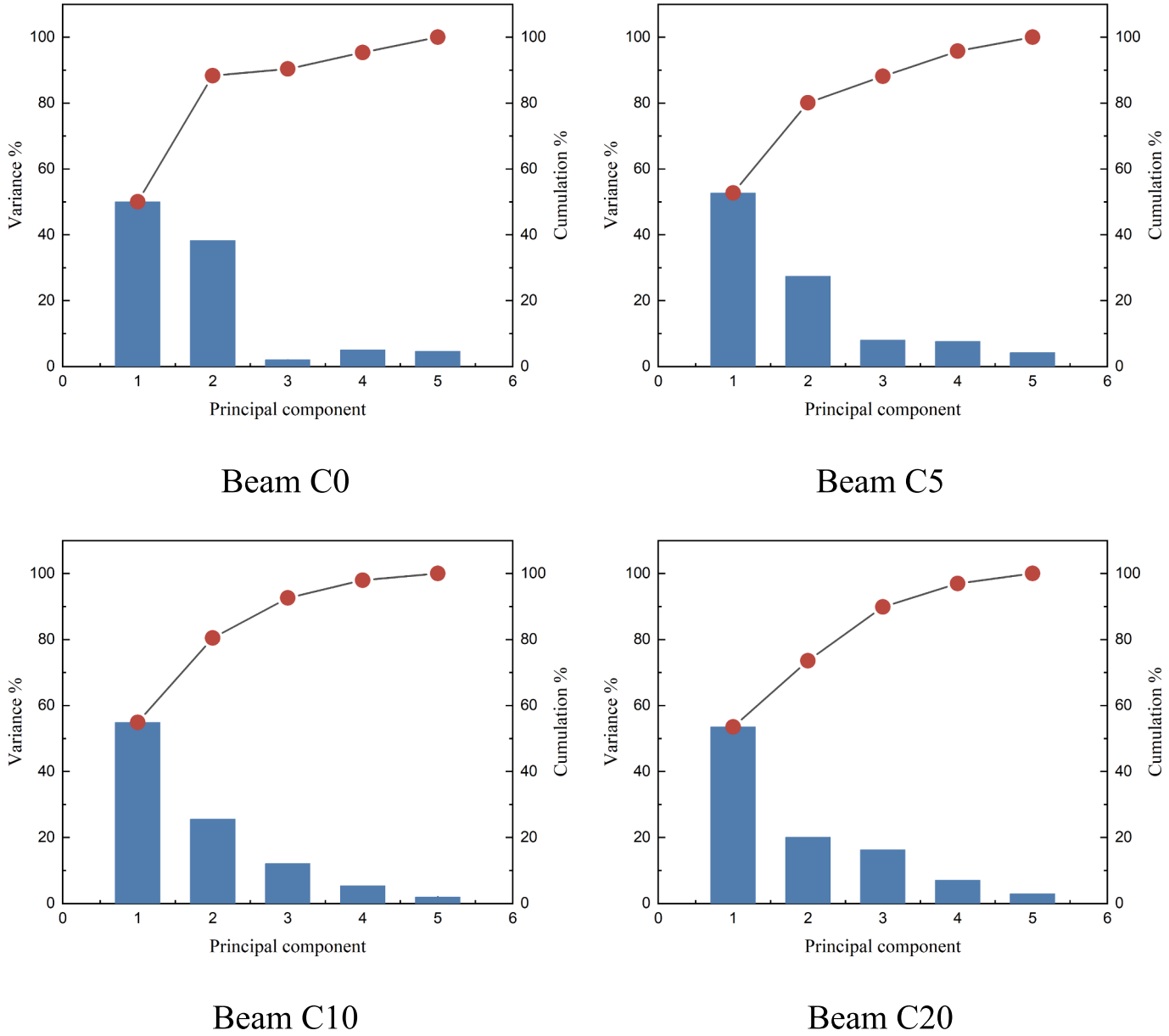

Fig. 6. The variance of principal components of specimens. The y axis on the right side shows the cumulative variances (a line in the graphs).

4.3. Choice of clusters number

Cluster analysis is a vital field of research that aims to determine the optimal number of clusters by assessing the results of clustering using computational indicators. In this study, we employ two evaluation indicators, namely the Silhouette Index (SI) and the Davies-Bouldin Index (DB), to evaluate the clustering results.

The Silhouette Index is calculated as the ratio of the distance between a data point and other data points within its cluster to the distance between the same data point and its nearest neighboring cluster [33]. A smaller Silhouette Index indicates that the distance between the cluster containing the data point and its nearest neighboring cluster is greater, implying better clustering results [18,36]. Mathematically, the Silhouette Index is defined as Eq.(9).

$$\mathrm{SC} = \frac{b(i) - a(i)}{\max\{a(i), b(i)\}} \tag{9}$$

where $a(i)$ is the average distance from point i to all other vectors in the same cluster, which measures the closeness of the AE data points in the cluster; $b(i)$ is the average distance from point i to vectors in other clusters, with the aim of finding the minimum value in the cluster.

Davies - Bouldin Index, proposed by David L. Davies and Donald Bouldin, an internal metric for evaluating the clustering algorithm. A smaller value of DB index indicated a smaller intra-class distance and a larger inter-class distance. The DB index is defined as Eq. (10).

$$DB = \frac{1}{k}\sum_{i=1}^{k} \max_{i\neq j, i,j\in[1,K]} \frac{s_i + s_j}{M_{ij}} \tag{10}$$

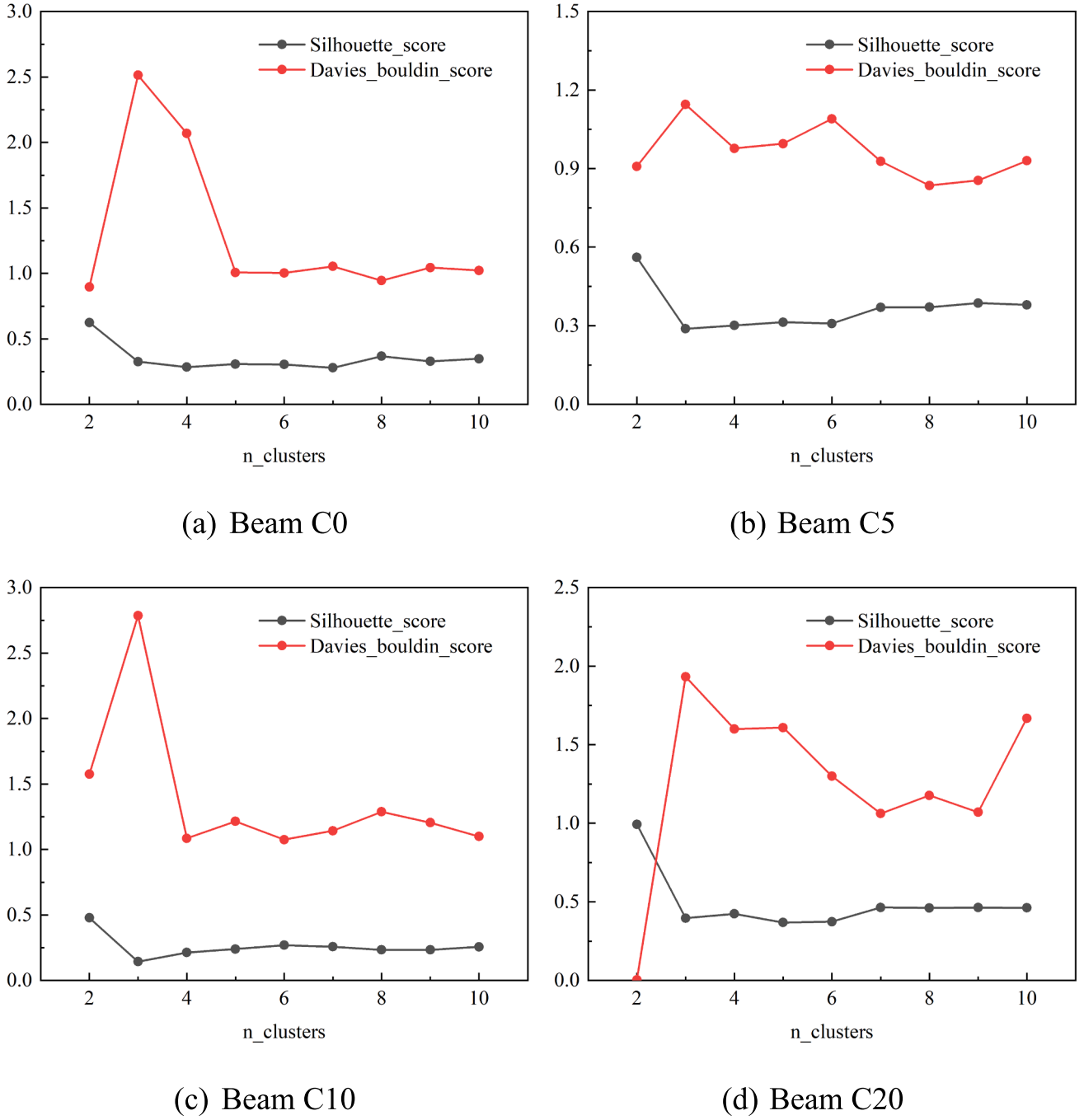

Fig. 7. The number of clusters evaluated by Silhouette coefficient and Davies–Bouldin index.

Where S_i, S_j denotes the dispersion of AE date points for i-th and j-th clusters; as shown in Eq. (11). M_{ij} is the distance between the center of i-th cluster and the center of j-th cluster, as shown in Eq. (12).

$$s_i = \left\{ \frac{1}{n} \sum_{j=1}^{n} \left| X_{ij} - A_i \right|^q \right\}^{\frac{1}{q}} \tag{11}$$

Where X_{ij} denotes the j-th data point in cluster i; A_i denotes the center of cluster i; n denotes the number of data points in cluster i; If q is taken as 1, it represents the mean of the distances from each point to the center; if q is taken as 2, it represents the standard deviation of the distances from each point to the center, and they can both be used to measure the degree of dispersion.

$$M_{ij} = \left\{ \sum_{k=1}^{K} \left| a_{ki} - a_{kj} \right|^q \right\}^{\frac{1}{q}} \tag{12}$$

Where a_{ki} denotes the value of the k-th attribute of the centroid of the i-th class.

It is worth noting that the Silhouette and Davies-Bouldin indices have different strengths and weaknesses. The Silhouette index is sensitive to the shape of the clusters and tends to favor convex clusters, while the Davies-Bouldin index is sensitive to the distance between clusters and tends to favor compact and well-separated clusters. Therefore, using both indices can provide a more robust evaluation of the clustering results.

Fig. 7 shows the evaluation of the number of clusters for four specimens using the Silhouette Index (SI) and the Davies - Bouldin Index (DB). It is worth noting that a higher Silhouette coefficient and a lower Davies-Bouldin index imply a better number of clusters. In order to determine the optimal number of clusters for the acoustic emission signals during the loading process, two clustering evaluation criteria were considered: the Davies-Bouldin index and the Silhouette coefficient. For beams C0, C5, and C10, both criteria indicated that the optimal number of clusters was K = 3. However, for beam C20, the Davies-Bouldin index suggested K = 3 while the Silhouette coefficient suggested K = 5. Taking both criteria into account, it was concluded that K = 3 was the optimal number of clusters for the AE signals during the loading process of CFRP reinforced corroded beams.

4.4. Clustering analysis using GMM

After parametric correlation analysis and principal component analysis, the AE signals were clustered using Gaussian mixture model algorithm. The withdrawal criterion for the end of the Gaussian mixture model clustering algorithm is a threshold value of 10^{-4} or a cumulative

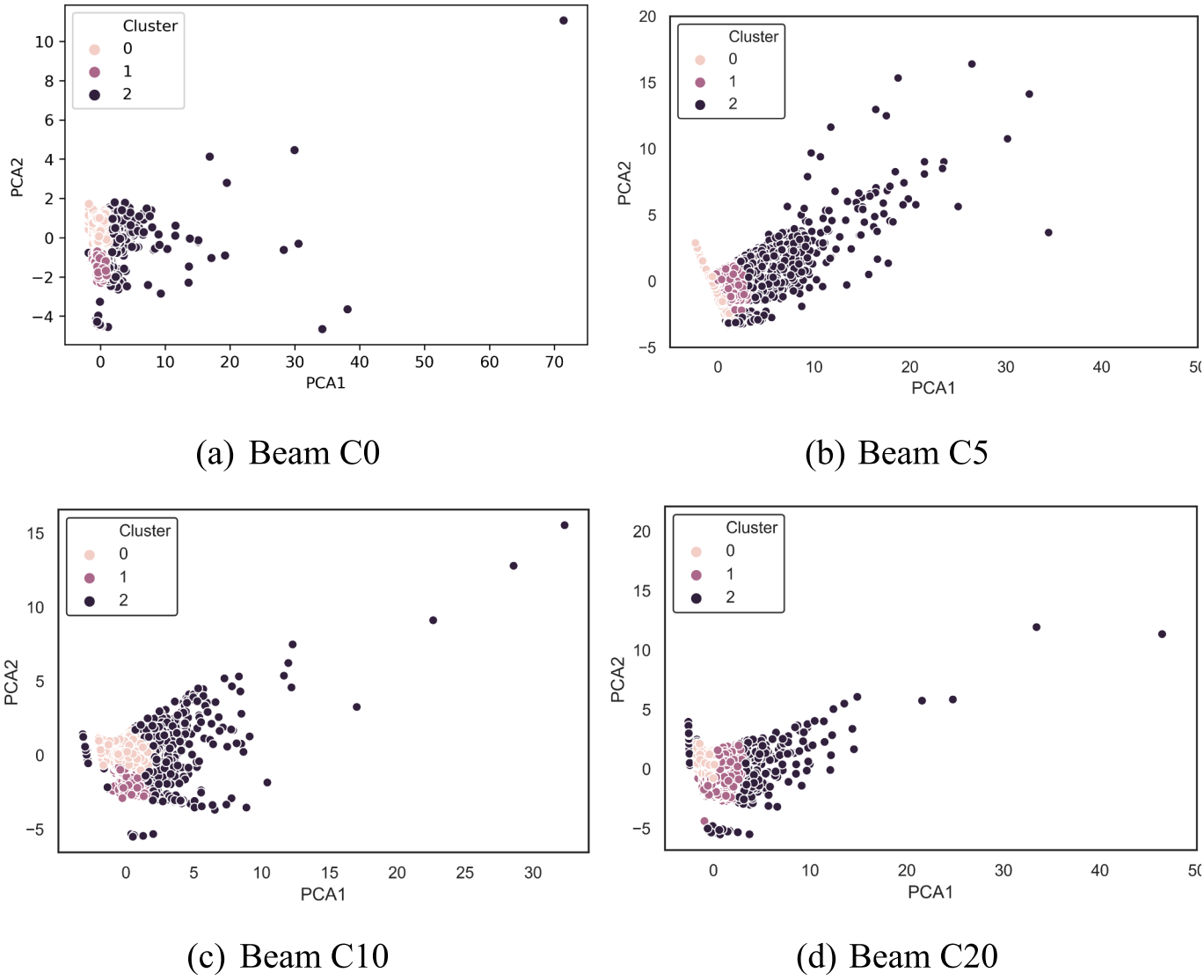

Fig. 8. Clustering along PCA axis of specimens.

number of iterations set to 1000. The AE data of 4 CFRP strengthened RC beams were dimensionality reduced into three clusters.

Fig. 8 shows the scatter plot of the AE signals collected during the loading process for all four specimens. PCA1 is represented along the x-axis, while PCA2 is represented along the y-axis. Each color in the scatter plot corresponds to a cluster obtained from the GMM algorithm. As can be seen from Fig. 8, the clustering results are well-distinguished, and each cluster represents a different type of AE signal generated during the loading process. Therefore, the results demonstrate the potential of using cluster analysis for damage pattern recognition in corroded steel beams strengthened with CFRP anchorage systems.

5. Results and discussion

5.1. Expectations of damage modes

The damage modes observed in corroded CFRP reinforced beams is a complex phenomenon influenced by several factors. Primarily, corrosion is a significant factor affecting the durability and strength of reinforced beams, resulting in reduced cross-sectional area of steel bars, increased surface roughness, and decreased bond strength between steel and concrete. These factors can lead to concrete spalling and cracking, ultimately causing a reduction in the beam's strength and stiffness. In addition to corrosion, steel bar slippage and concrete plastic deformation during the loading process of CFRP reinforced beams can also impact the beam's strength and stiffness. Steel bar slippage can lead to the failure of the bond between concrete and steel, causing further damage. Meanwhile, concrete plastic deformation can increase the beam's deformation, resulting in additional cracks.

Fig. 9 depicts the final failure modes of corroded beams strengthend by CFRP anchorage system. It can be observed that debonding, tearing, and fracture at the interface between CFRP and the beam can occur during the failure process of CFRP reinforced beams.interface can occur during the failure process of CFRP reinforced beams. When the stress on the beam surpasses the ultimate strength of CFRP, the CFRP laminate may tear and fracture, resulting in beam failure. Debonding can also occur at the interface between CFRP and the beam, decreasing the beam's strength and stiffness. Lastly, microcracks' initiation and propagation inside the beam are also observed in the damage pattern of CFRP reinforced corroded beams. Microcracks' initiation and propagation can be caused by several factors, such as corrosion, concrete cracking, and steel bar corrosion. As these microcracks extend to the surface of the beam, they form macrocracks, resulting in beam failure.

The main damage patterns vary across different periods, and multiple damage patterns can occur simultaneously. Due to the lack of prior knowledge of signal characteristics associated with each failure mechanism and the absence of micro-scale evidence confirming the existence of specific damage patterns, principal component clustering was employed to separate the data representing three damage patterns identified by the acoustic emission (AE) feature parameters. The results of the three clusters corresponded to the damage modes of concrete matrix damage, CFRP debonding, and CFRP tearing, providing a robust data foundation for subsequent analysis.

5.2. Expectations and results of AE clustering

The AE clustering analysis was conducted to identify the damage patterns in corroded beams strengthened by CFRP anchorage system. The three clusters were obtained through principal component analysis and Gaussian mixture model clustering algorithm. In this section, we will discuss the expectations and results of AE clustering based on the analysis of the AE parameters of the three clusters.

Table 2 - 4 present the mean values of the rise time, ring count, amplitude, absolute energy, duration, and peak frequency for each cluster. As expected, the AE parameters of the three clusters showed distinct differences. Cluster 0 had the shortest rise time of 132 μs, the lowest ring count of 21, and the lowest absolute energy of 1053 mV^2s, indicating a shorter duration of the AE signal and less AE sources. It also had the shortest duration of 550 μs and the highest peak frequency of 77 kHz, suggesting a higher frequency range of the AE signal. Cluster 1 had intermediate values for all parameters, with a rise time of 500 μs, a ring count of 88, an amplitude of 60 dB, an absolute energy of 5.8 $\times 10^6$ mV^2s, a duration of 2651 μs, and a peak frequency of 65 kHz. The acoustic emission parameters of cluster 1 were in between those of cluster 0 and cluster 2. Cluster 2 had the longest rise time of 1267 μs and the highest ring count of 503, indicating a longer duration of the AE signal and more AE sources. It also had the highest absolute energy of 4.8 $\times 10^8$ mV^2s and the longest duration of 30277 μs, suggesting a large amount of energy released during the damage process. In terms of frequency, cluster 2 had the lowest peak frequency of 32 kHz, indicating a lower frequency range of the AE signal.

The peak frequency showed a decreasing trend from cluster 0 to cluster 2, whereas other parameters showed an increasing trend. Among them, the absolute energy showed the largest increase trend, and the amplitude and ring count also showed a significant increase trend. It is very obvious that cluster 0 showed the characteristics of low frequency and high energy, while cluster 2 showed the characteristics of high frequency and low energy.

5.3. Association of clusters to damage modes

Based on the clustering results, the next step was to associate the identified clusters with the expected damage modes. The three clusters were assigned to three damage modes: concrete matrix damage, CFRP-matrix debonding, and CFRP tearing. The identification of the damage modes was based on the analysis of AE feature parameters, which provided a clear separation of the different types of signals associated with each damage mode.

Cluster 0 was associated with concrete matrix damage, characterized by the presence of low-amplitude AE signals with a high frequency content. The analysis of AE feature parameters revealed a significant number of short-duration, high-frequency events within this cluster. These signals were primarily generated by the micro-cracking occurring within the concrete matrix as a result of the applied load on the corroded beam. The loss of bond between the reinforcement and the concrete was a critical contributing factor to the initiation and propagation of cracks in the concrete matrix. This mode of damage poses a significant threat to the overall structural integrity of the CFRP-strengthened beam, as it weakens the load-bearing capacity of the structure and may lead to progressive deterioration if not addressed promptly.

Cluster 1 was associated with CFRP-matrix debonding, characterized by the presence of high-amplitude AE signals with a low frequency content. The AE feature parameters analysis revealed a considerable number of long-duration, low-frequency events within this cluster. These signals were primarily generated by the debonding of the CFRP sheets from the surface of the corroded beam. CFRP-matrix debonding is a critical mode of damage that undermines the effectiveness of the reinforcement in carrying the applied load. If left untreated, this damage mode can lead to a significant reduction in the load-carrying capacity of the structure, compromising its overall stability and safety.

Cluster 2 was associated with CFRP tearing, characterized by the presence of high-amplitude AE signals with a low peak frequency content. The AE feature parameters analysis revealed a high number of high-energy, low-peak-frequency events within this cluster, confirming the presence of CFRP tearing. The signals were primarily generated by the tearing of the CFRP sheets due to the excessive tensile stress induced by the applied load. CFRP tearing is a critical mode of damage that directly affects the load-carrying capacity of the CFRP reinforcement. It can lead to sudden structural failure if not detected and addressed in a timely manner.

The association of the identified clusters with the specific damage

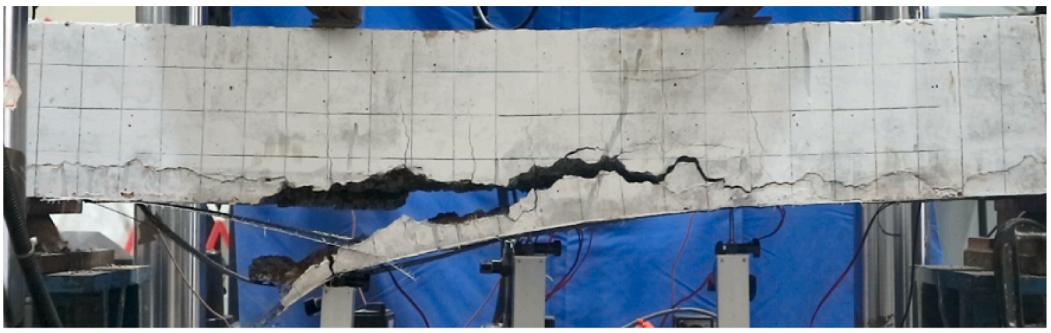

(a) Beam C0

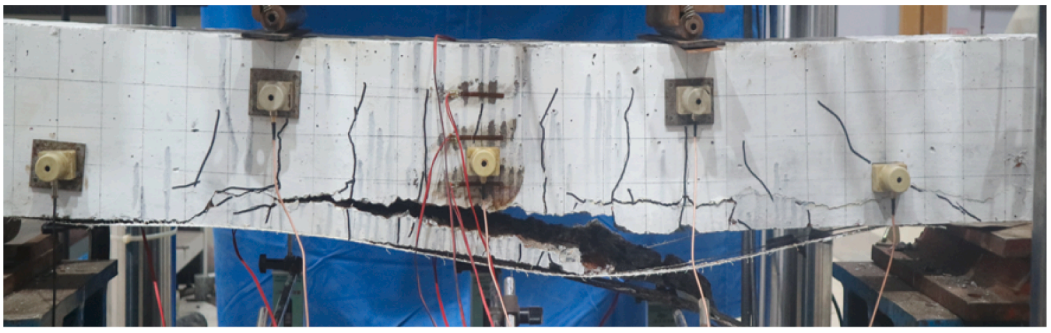

(b) Beam C5

(c) Beam C10

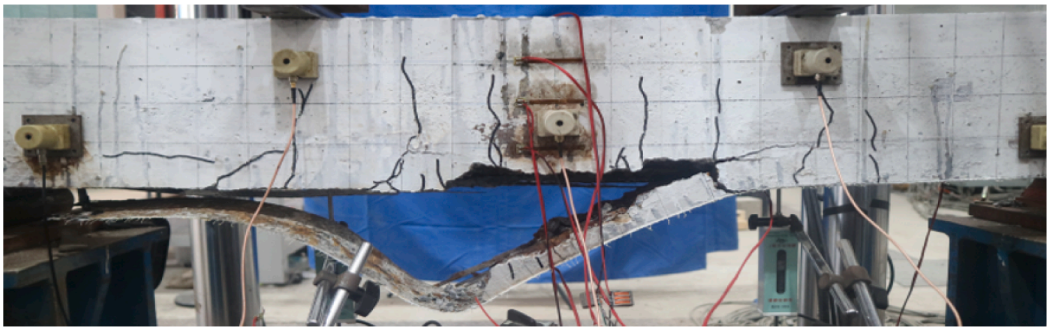

(d) Beam C20

Fig. 9. The final failure modes of test beams.

Table 2
Feature statistics of cluster 0.

Cluster 0 Specimen	Rise time	Ring counts	Duration	Amplitude	Absolute energy	Peak frequency
C0	100	21	461	48	1889	96
C5	129	16	469	46	383	68
C10	123	21	537	47	914	78
C20	176	26	733	46	1028	67
Average	132	21	550	47	1053	77

Table 3
Feature statistics of cluster 1.

Cluster 1 Specimen	Rise time	Ring counts	Duration	Amplitude	Absolute energy	Peak frequency
C0	235	66	1601	60	2.8×10^{6}	76
C5	273	54	1582	56	7.0×10^{5}	53
C10	617	88	3219	63	8.0×10^{6}	58
C20	873	143	4203	63	1.2×10^{7}	72
Average	500	88	2651	60	5.9×10^{6}	65

Table 4
Feature statistics of cluster 2.

Cluster 2 Specimen	Rise time	Ring counts	Duration	Amplitude	Absolute energy	Peak frequency
C0	298	198	16,414	94	4.1×10^{8}	37
C5	1209	823	39,340	89	3.0×10^{8}	34
C10	1635	342	23,563	95	4.1×10^{8}	24
C20	1927	650	41,792	97	7.8×10^{8}	34
Average	1267	503	30,277	94	4.8×10^{8}	32

modes provided valuable insights into the structural behavior of the CFRP-strengthened beam under different loading conditions. The load-time analysis for each cluster offered a comprehensive understanding of how the damage modes influenced the overall structural performance. Moreover, real-time monitoring of the CFRP-strengthened beam allowed for the early detection of damage initiation and progression, enabling timely intervention and maintenance actions.

5.4. Analysis of failure mechanisms for CFRP-reinforced beams

In the previous section, unsupervised identification methods were used to distinguish the three types of damage mechanisms in the specimens and obtain reasonable classification results. Next, these results will be used to examine the AE activity characteristics and damage failure process of the CFRP strengthened beams.

As shown in Fig. 10, AE signals appeared almost at the beginning of the loading process. From the total activity level of the three types of AE signals, the damage process can be roughly divided into three stages: the initial damage stage, damage development stage, the continuous damage growth stage. During the initial damage stage, fewer low-intensity AE signals are detected, which can be attributed to the fact that under the action of the applied load, voids in the concrete may undergo shrinkage or collapse, resulting in small displacements and deformations that trigger AE signals. At the damage development stage (from the rapid increase point of the cumulative AE hits curve to the yield point), where there is a significant increase in signals related to concrete matrix damage and CFRP-matrix debonding, while signals related to CFRP tearing remain relatively low level of increase. This indicates that during this stage, the damage in the concrete begins to propagate, leading to larger cracks and localized failure zones. As the load increases, the FRP continues to bear tension in the concrete beam. Near the damaged concrete region, there may be phenomena such as interface shearing and stress redistribution in the sensitive area, which can result in minor interface shearing and stress release, thereby triggering acoustic emission (AE) signals. At the continuous damage growth stage (i.e., from the beginning of steel yielding up to the final failure), As the beam approaches or reaches the failure load, there is a significant increase in the proportion of AE signals associated with different damage modes. This is because at this stage, the damage modes such as concrete matrix failure, debonding between the FRP and concrete matrix, and tearing of the FRP intensify, resulting in a higher occurrence of AE events.

Fig. 11 illustrates the Cumulative Energy and Load vs. Time curves for the various damage modes observed in the test beam. The Cumulative Energy curve represents the accumulated energy release during the loading process, while the Load vs. Time curve depicts the applied load over time. The different damage modes, including concrete damage, CFRP -matrix debonding, and CFRP tearing, are evident from the distinct patterns in the Cumulative Energy curves.

Based on the observations from the Fig. 11, it can be observed that signals related to matrix cracking are produced relatively steadily throughout the entire damage process, indicating that matrix deformation damage is a gradual process. These signals account for 60—80% of the total AE signals produced and are one of the more important damage mechanisms in CFRP strengthened beams. Furthermore, it is evident that as the degree of corrosion increases, the cumulative energy resulting from concrete damage decreases. This can be attributed to several factors. Firstly, when the degree of corrosion is lower, the concrete matrix retains higher strength. As a result, it can withstand greater stress during loading, leading to increased energy release during concrete damage. Additionally, a lower degree of corrosion also indicates a more uniform stress distribution within the concrete matrix, resulting in a more uniform release of energy and higher cumulative AE energy.

Observations from the Fig. 11 indicate that there is an inverse relationship between the degree of corrosion and the acoustic emission (AE) energy generated during CFRP debonding. Specifically, as the degree of corrosion increases, the AE energy generated during CFRP debonding

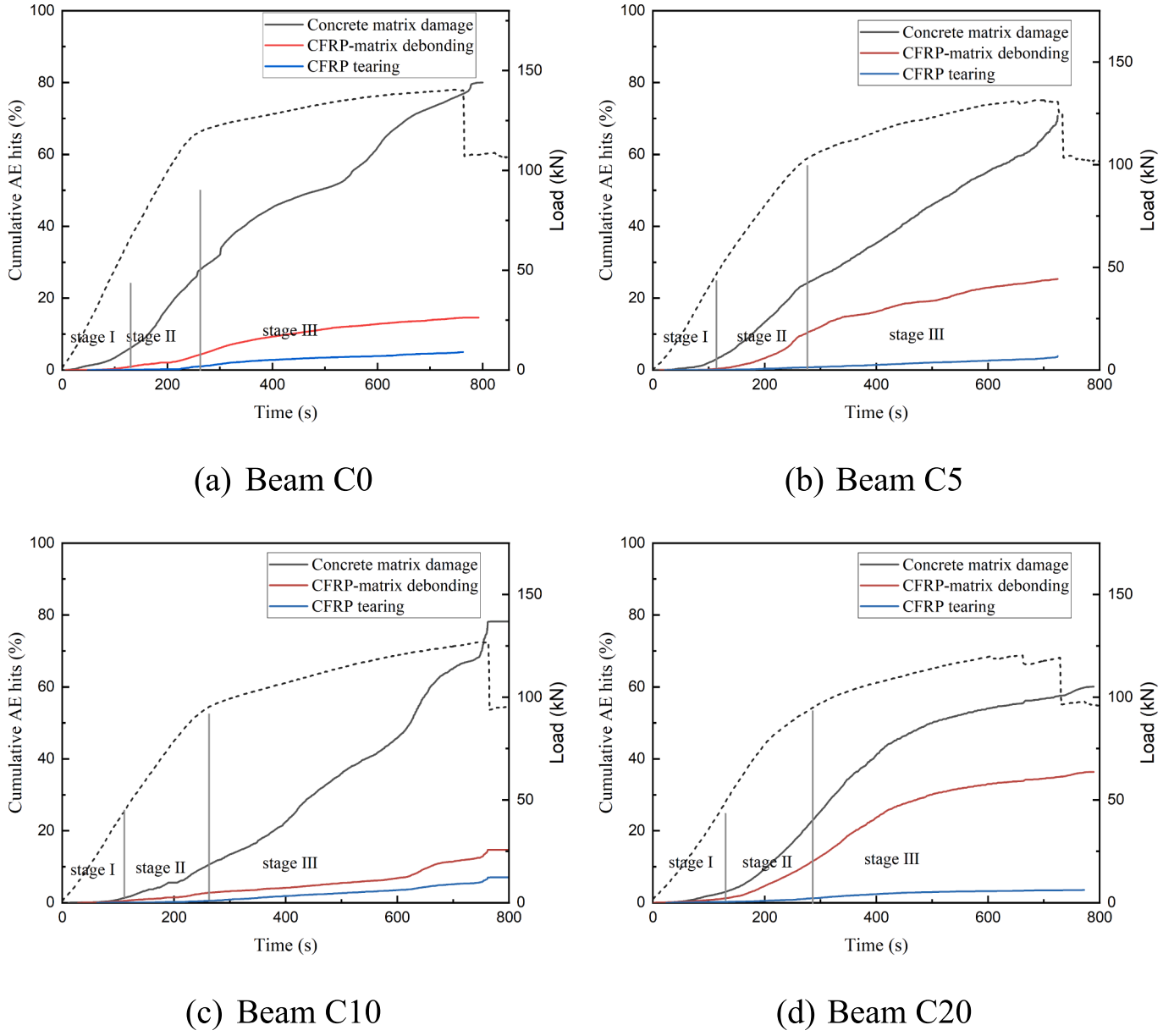

Fig. 10. Cumulative AE hits ratio and Load vs. Time curves for different damage modes of the test beams.

decreases. This phenomenon can be attributed to two main factors. Firstly, the decrease in interfacial bond strength between the concrete and CFRP due to the presence of surface corrosion cracks. Weaker bond strength makes it easier for the CFRP to detach from the concrete surface during delamination. As a result, the reduced bond strength leads to a decrease in the energy released at the debonding interface, resulting in lower cumulative AE energy. Secondly, the presence of corrosion cracks may complicate the crack propagation path during CFRP – matrix debonding. The crack propagation path refers to the direction or route that a crack takes as it extends or grows within a material. The variation in crack propagation path can affect the mode and extent of energy release. If corrosion cracks exist and intertwine with the delamination process, it can result in discontinuous or dispersed energy release, leading to a decrease in cumulative AE energy.

Signals related to CFRP tearing account for 5–15% of the total AE signals produced, and their signals increase suddenly in the final stage of tensile, indicating that the specimen experienced serious fiber rupture, which is the main cause of failure. Although the count of CFRP tearing events is relatively low, the cumulative energy released during these events is significant. This can be attributed to the nature of energy release in CFRP tearing processes. During CFRP tearing, the tearing and rupture of the fibers and interfacial shearing result in a greater amount of energy conversion and transfer. These processes involve more complex energy dissipation mechanisms compared to the relatively smaller energy release associated with CFRP debonding, which mainly occurs due to the failure of the bonding interface. Moreover, CFRP tearing typically occurs at multiple locations and levels, exhibiting complex crack propagation paths. These complexities and variations contribute to the release of a higher amount of energy during CFRP tearing events.

6. Conclusions

In conclusion, this study demonstrated the effectiveness of using acoustic emission (AE) techniques for damage pattern recognition of corroded beams strengthened by CFRP anchorage. The results showed that AE monitoring can provide valuable information on the damage evolution process and failure mechanisms of the CFRP-reinforced beams. Based on the experimental study, the following conclusions

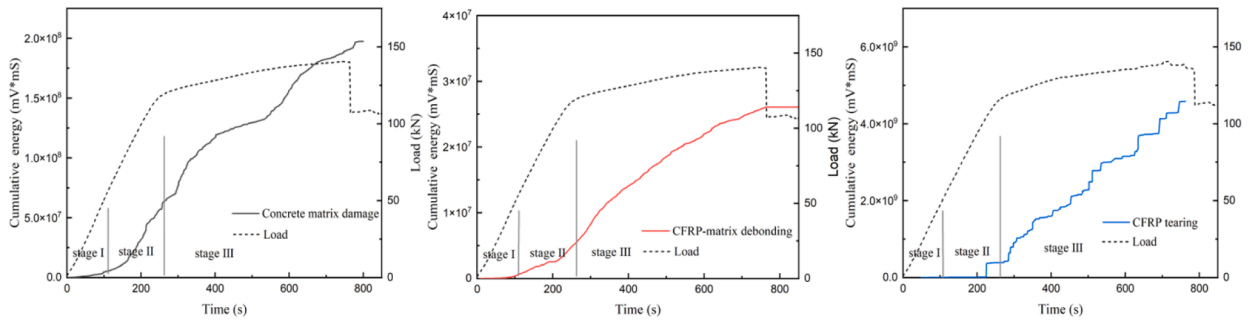

(a) Beam C0

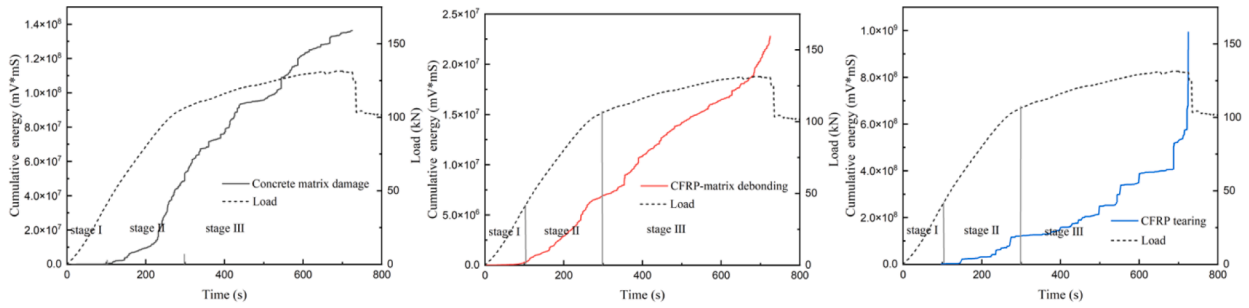

(b) Beam C5

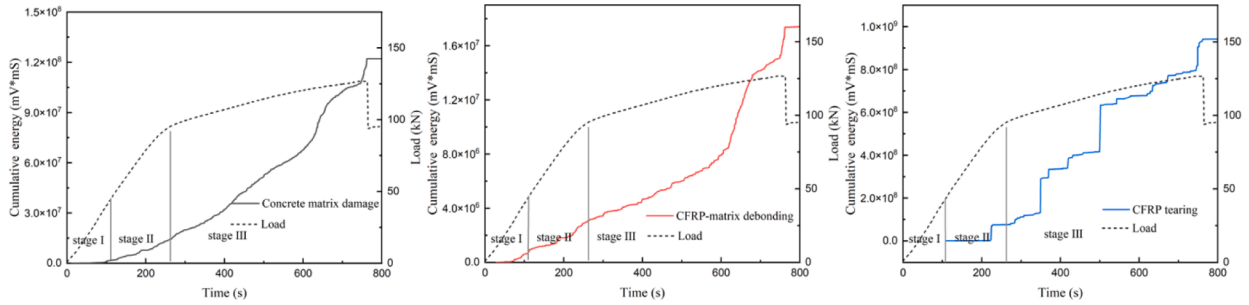

(c) Beam C10

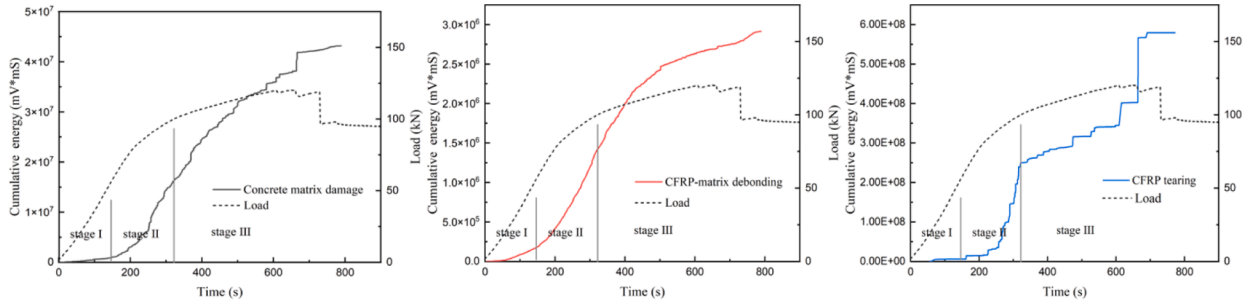

(d) Beam C20

Fig. 11. Cumulative Energy and Load vs. Time curves for different damage modes of the test beams.

can be drawn:

(1) Four corroded beams strengthened by CFRP anchorage system were tested with flexural loads and monitored using AE technique. Three major failure modes were observed in the specimens, i.e., concrete matrix damage, CFRP debonding, and CFRP tearing.
(2) The proposed pattern recognition method was applied on the collected AE data. The AE signals exhibited distinct characteristics for different damage modes: concrete matrix damage had high-frequency and low-energy characteristics, CFRP-matrix debonding showed intermediate values for all parameters, and CFRP tearing had longer durations, lower peak frequencies, and high-energy characteristics. The results demonstrate the effectiveness of AE clustering in identifying different damage modes and reveal a clear relationship between AE parameters and the identified patterns.
(3) The analysis of AE signals revealed that the damage process in the tested beams can be divided into three stages, with an initial stage showing fewer low-intensity AE signals, a damage development stage characterized by an increase in concrete-matrix damage and CFRP – matrix debonding signals, and a continuous damage growth stage marked by a significant increase in AE signals associated with three damage modes.
(4) For CFRP-strengthened corroded concrete beams, the degree of corrosion significantly affects the cumulative acoustic emission (AE) energy and damage patterns.
   - Lower degrees of corrosion result in higher cumulative energy from concrete damage, and the concrete damage exhibits a gradual development process.
   - In the CFRP debonding process, an increase in the degree of corrosion leads to a decrease in the cumulative AE energy. This can be attributed to the reduced bond strength between the concrete and CFRP caused by surface corrosion cracks, making it easier for the CFRP to detach from the concrete surface during debonding. Additionally, the presence of corrosion cracks may complicate the crack propagation path during CFRP-matrix debonding, affecting the mode and extent of energy release.
   - CFRP tearing generates a high cumulative AE energy despite the relatively low frequency of tearing events. This can be attributed to the complex energy conversion and transfer mechanisms involved in the tearing and rupture of fibers and interfacial shearing.

Overall, the results of this study can provide valuable guidance for the design and evaluation of CFRP anchorage systems for the rehabilitation of corroded structures. The use of AE techniques for damage pattern recognition can improve the understanding of the damage mechanism and contribute to the development of more effective maintenance strategies.

CRediT authorship contribution statement

Tanbo Pan: Writing – review & editing, Methodology, Investigation, Conceptualization. **Yonglai Zheng:** Supervision, Funding acquisition. **Yubao Zhou:** Methodology, Investigation. **Wenbin Luo:** Investigation, Resources. **Xubing Xu:** Methodology, Investigation. **Chenyu Hou:** Methodology, Investigation. **Yujue Zhou:** Resources.

Declaration of Competing Interest

The authors declare that they have no known competing financial interests or personal relationships that could have appeared to influence the work reported in this paper.

Data availability

The authors do not have permission to share data.

Acknowledgments

The authors are grateful for the financial support from the National Science Foundation of Fujian Province (No.2022 J011185).

References

[1] S. Ahmad, Reinforcement corrosion in concrete structures, its monitoring and service life prediction - a review, Cement Concrete Comp 25 (4–5) (2003) 459–471, https://doi.org/10.1016/S0958-9465(02)00086-0.
[2] A.A. Almusallam, Effect of degree of corrosion on the properties of reinforcing steel bars, Construction and Building Materials 15 (8) (2001) 361–368, https://doi.org/10.1016/S0950-0618(01)00009-5.
[3] E. Lozinguez, J.F. Barthelemy, V. Bouteiller, T. Desbois, Contribution of sacrificial anode in reinforced concrete patch repair: Results of numerical simulations, Construction and Building Materials 178 (2018) 405–417, https://doi.org/10.1016/j.conbuildmat.2018.05.063.
[4] R.A. Maleki, A. Hattori, H. Kawano, M. Risa, Characteristics of Patch-Repaired RC under influenced of chloride ions, American Institute of Physics Conference Proceedings 2017 (1835), 020014, https://doi.org/10.1063/1.4981836.
[5] I. Ortega, T.M. Pellicer, P.A. Calderon, J.M. Adam, Cement-based mortar patch repair of RC columns, Comparison with all-four-sides and one-side repair, Constr Build Mater 186 (2018) 338–350, https://doi.org/10.1016/j.conbuildmat.2018.07.148.
[6] G.G. Triantafyllou, T.C. Rousakis, A.I. Karabinis, Corroded RC beams patch repaired and strengthened in flexure with fiber-reinforced polymer laminates, Compos Part B-Eng 112 (2017) 125–136, https://doi.org/10.1016/j.compositesb.2016.12.032.
[7] T.B. Pan, Y.L. Zheng, Y.J. Zhou, Y.C. Liu, K.L. Yu, Y.B. Zhou, Coupled effects of corrosion damage and sustained loading on the flexural behavior of RC beams strengthened with CFRP anchorage system, Composite Structures 289 (2022), 115416, https://doi.org/10.1016/j.compstruct.2022.115416.
[8] Y.L. Zheng, Y.J. Zhou, Y.B. Zhou, T.B. Pan, Q. Zhang, D. Liu, Cracking behavior of reinforced concrete beams strengthened with CFRP anchorage system under cyclic and monotonic loading, Engineering Structures 207 (2020), 110222, https://doi.org/10.1016/j.engstruct.2020.110222.
[9] R.Z. Alrousan, B.R. Alnemrawi, Punching shear behavior of FRP reinforced concrete slabs under different opening configurations and loading conditions, Case Stud Constr Mat 17 (2022) e01508.
[10] R. Capozucca, E. Magagnini, E. Bettucci, Delamination buckling of GFRP-strips in strengthened RC beams, Composite Structures 300 (2022), 116183, https://doi.org/10.1016/j.compstruct.2022.116183.
[11] N. Li, W.S. Tang, X.Y. Chen, K. Wang, S. Li, Compressive behavior degradation of FRP-confined RC columns exposed to a chlorine environment, Marine Structures 86 (2022), 103277, https://doi.org/10.1016/j.marstruc.2022.103277.
[12] S. Tayfur, N. Alver, H.M. Tanarslan, E. Ercan, Identifying CFRP strip width influence on fracture of RC beams by acoustic emission, Construction and Building Materials 164 (2018) 864–876, https://doi.org/10.1016/j.conbuildmat.2018.01.189.
[13] H. Abbas, H. Elsanadedy, L. Alaoud, T. Almusallam, Y. Al-Salloum, Effect of confining stirrups and bar gap in improving bond behavior of glass fiber reinforced polymer (GFRP) bar lap splices in RC beams, Construction and Building Materials 365 (2023), 129943, https://doi.org/10.1016/j.conbuildmat.2022.129943.
[14] M.G. Sohail, M. Wasee, N. Al Nuaimi, W. Alnahhal, M.K. Hassan, Behavior of artificially corroded RC beams strengthened with CFRP and hybrid CFRP-GFRP laminates, Engineering Structures 272 (2022), 114827, https://doi.org/10.1016/j.engstruct.2022.114827.
[15] J.S. Wang, J.A. Niu, Z.H. Xiang, J. Zhou, J. Wang, Acoustic emission assessment of corroded RC columns jointly reinforced with concrete canvas and CFRP, Coatings 12 (12) (2022) 1843, https://doi.org/10.3390/coatings12121843.
[16] W.W. Wu, X.J. He, Y.I. Shah, J. He, W.R. Yang, Long-term bond degradation of GFRP-RC beams in the complex alkaline environment for eight years, Composite Structures 299 (2022), 116093, https://doi.org/10.1016/j.compstruct.2022.116093.
[17] J.F. Bonacci, M. Maalej, Behavioral trends of RC beams strengthened with externally bonded FRP, Journal of Composites for Construction 5 (2) (2001) 102–113, https://doi.org/10.1061/(Asce)1090-0268(2001)5:2(102).
[18] S.F. Karimian, M. Modarres, Acoustic emission signal clustering in CFRP laminates using a new feature set based on waveform analysis and information entropy analysis, Composite Structures 268 (2021), 113987, https://doi.org/10.1016/j.compstruct.2021.113987.
[19] J. Skoczylas, M. Klonica, S. Samborski, A study on the FRP composite's matrix damage resistance by means of elastic wave propagation analysis, Composite Structures 297 (2022), 115935, https://doi.org/10.1016/j.compstruct.2022.115935.
[20] Z. Xia, Q.L. Yao, X.H. Li, L.L. Yu, C.H. Shan, Y. Li, Y.S. Hao, Acoustic emission characteristics and energy mechanism of CFRP-jacketed coal specimens under uniaxial compression, Construction and Building Materials 342 (2022), 127936, https://doi.org/10.1016/j.conbuildmat.2022.127936.

[21] Y.L. Zheng, Y. Wen, T.B. Pan, Y.C. Liu, Y.J. Zhou, R.Z. Li, Y.B. Zhou, Fractal characteristics and damage evaluation of corroded beams under four-point bending tests based on acoustic emission techniques, Measurement 202 (2022), 111792, https://doi.org/10.1016/j.measurement.2022.111792.
[22] F.J. Rescalvo, A. Aguilar-Aguilera, E. Suarez, I. Valverde-Palacios, A. Gallego, Acoustic emission during wood-CFRP adhesion tests, International Journal of Adhesion and Adhesives 87 (2018) 79–90, https://doi.org/10.1016/j.ijadhadh.2018.09.007.
[23] M. Saeedifar, M.N. Saleh, S.T. De Freitas, D. Zarouchas, Damage characterization of adhesively-bonded bi-material joints using acoustic emission, Compos Part B-Eng 176 (2019), 107356, https://doi.org/10.1016/j.compositesb.2019.107356.
[24] Y. Tang, Y.Z. Guo, X.D. Chen, Z. Wang, Y. Wei, Acoustic emission characteristics of concrete cylinders reinforced with steel-fiber-reinforced composite bars under uniaxial compression, J Build Eng 59 (2022), 105074, https://doi.org/10.1016/j.jobe.2022.105074.
[25] S. Degala, P. Rizzo, K. Ramanathan, K.A. Harries, Acoustic emission monitoring of CFRP reinforced concrete slabs, Construction and Building Materials 23 (5) (2009) 2016–2026, https://doi.org/10.1016/j.conbuildmat.2008.08.026.
[26] S. Barre, M.L. Benzeggagh, On the use of Acoustic-Emission to investigate damage mechanisms in Glass-Fiber-Reinforced polypropylene, Composites Science and Technology 52 (3) (1994) 369–376, https://doi.org/10.1016/0266-3538(94)90171-6.
[27] S. Shahidan, R. Pullin, K.M. Holford, B.N. Muhamad, N.N. Md, Quantitative evaluation of the relationship between tensile crack and shear movement in concrete beams, Adv Mater Res-Switz 626 (2012) 355-+, https://doi.org/10.4028/www.scientific.net/AMR.626.355.
[28] Y.H. Yu, J.H. Choi, J.H. Kweon, D.H. Kim, A study on the failure detection of composite materials using an acoustic emission, Composite Structures 75 (1–4) (2006) 163–169, https://doi.org/10.1016/j.compstruct.2006.04.070.
[29] P.J. deGroot, P.A.M. Wijnen, R.B.F. Janssen, Real-time frequency determination of acoustic emission for different fracture mechanisms in carbon epoxy composites, Composites Science and Technology 55 (4) (1995) 405–412, https://doi.org/10.1016/0266-3538(95)00121-2.
[30] S. Tayfur, T.H. Zhang, M. Mahdi, M. Issa, D. Ozevin, Cluster-based sensor selection framework for acoustic emission source localization in concrete, Measurement 219 (2023), 113293, https://doi.org/10.1016/j.measurement.2023.113293.
[31] S. Tayfur, N. Alver, S. Abdi, S. Saatci, A. Ghiami, Characterization of concrete matrix/steel fiber de-bonding in an SFRC beam: Principal component analysis and k-mean algorithm for clustering AE data, Engineering Fracture Mechanics 194 (2018) 73–85, https://doi.org/10.1016/j.engfracmech.2018.03.007.
[32] M. Johnson, Waveform based clustering and classification of AE transients in composite laminates using principal component analysis, NDT and E International 35 (6) (2002) 367–376, https://doi.org/10.1016/S0963-8695(02)00004-X.
[33] N. Pei, S.Y. Zhou, C.U. Xu, J.J. Shang, Q. Wu, Cluster analysis of acoustic emission signals for tensile damage characterization of quasi-static indented carbon/glass fiber-reinforced hybrid laminate composites, Compos Part a-Appl S 150 (2021), 106597, https://doi.org/10.1016/j.compositesa.2021.106597.
[34] Y.E. Guo, D.G. Shang, L.X. Zuo, L.F. Qu, G. Hou, D. Cai, T. Jin, X. Yin, Identification of fatigue damage modes for carbon fiber/epoxy composites using acoustic emission monitoring under fully reversed loading, Polym Composite 43 (6) (2022) 3371–3385, https://doi.org/10.1002/pc.26622.
[35] M.G.R. Sause, A. Gribov, A.R. Unwin, S. Horn, Pattern recognition approach to identify natural clusters of acoustic emission signals, Pattern Recognition Letters 33 (1) (2012) 17–23, https://doi.org/10.1016/j.patrec.2011.09.018.
[36] F.Z. Du, D.S. Li, D.P. Qiu, Cluster analysis and damage identification for FRP/steel-confined RC column using AE technique, Smart Structures and Systems 27 (3) (2021) 407–419. https://doi.org/10.12989/sss.2021.27.3.407.
[37] A. Nair, C.S. Cai, X. Kong, Acoustic emission pattern recognition in CFRP retrofitted RC beams for failure mode identification, Compos Part B-Eng 161 (2019) 691–701, https://doi.org/10.1016/j.compositesb.2018.12.120.
[38] A. Nair, C.S. Cai, X. Kong, Using acoustic emission to monitor failure modes in CFRP-Strengthened concrete structures, J Aerospace Eng 33 (1) (2020) 04019110, https://doi.org/10.1061/(Asce)As.1943-5525.0001106.
[39] A. International, ASTM C192/C192M-19, standard practice for making and curing concrete test specimens in the laboratory, American Society of testing Materials (2019).
[40] S.L. Orton, J.O. Jirsa, O. Bayrak, Design considerations of carbon fiber anchors, Journal of Composites for Construction 12 (6) (2008) 608–616, https://doi.org/10.1061/(Asce)1090-0268(2008)12:6(608).
[41] P.V. Llaurado, J. Fernandez-Gomez, F.J.G. Ramos, Influence of geometrical and installation parameters on performance of CFRP anchors, Composite Structures 176 (2017) 105–116, https://doi.org/10.1016/j.compstruct.2017.05.035.
[42] International Organization for Standardization (2019).
[43] F.Q. Zhang, Y.G. Yang, S.A.A.M. Fennis, M.A.N. Hendriks, Developing a new acoustic emission source classification criterion for concrete structures based on signal parameters, Construction and Building Materials 318 (2022), 126163, https://doi.org/10.1016/j.conbuildmat.2021.126163.
[44] E. Ramasso, T. Denoeux, G. Chevallier, Clustering acoustic emission data streams with sequentially appearing clusters using mixture models, Mech Syst Signal Pr 181 (2022), ARTN , https://doi.org/10.1016/j.ymssp.2022.109504.
[45] M.M. Nkogo, E. Ramasso, P. Le Moal, G. Bourbon, A variational bayesian clustering approach to acoustic emission interpretation including soft labels, Belief Functions: Theory and Applications (Belief 13506 (2022) (2022) 23–32, https://doi.org/10.1007/978-3-031-17801-6_3.
[46] J.J. Sun, X. Chen, Z.W. Fu, G. Lacidogna, Damage pattern recognition and crack propagation prediction for crumb rubber concrete based on acoustic emission techniques, Appl Sci-Basel 11 (23) (2021) 11476, https://doi.org/10.3390/app112311476.
[47] G.B. Lucas, B.A. De Castro, J.A. Ardila-Rey, A. Glowacz, J.V.F. Leao, A.L. Andreoli, A novel approach applied to transient Short-Circuit diagnosis in TIMs by piezoelectric sensors, PCA, and Wavelet Transform, Ieee Sens J 23 (8) (2023) 8899–8908, https://doi.org/10.1109/Jsen.2023.3252816.
[48] H. Mahajan, S. Banerjee, Quantitative investigation of acoustic emission waveform parameters from crack opening in a rail section using clustering algorithms and advanced signal processing, Sensors-Basel 22 (22) (2022) 8643, https://doi.org/10.3390/s22228643.
[49] W.G. Wu, W. Wei, Y.J. Wang, A.X. Sha, W.F. Hao, Monitoring damage progression in tensile tested SiCp/Al composites using acoustic emission, Frontiers in Materials 9 (2022), 918091, https://doi.org/10.3389/fmats.2022.918091.